

Dual energy computed tomography for explosive detection

Zhengrong Ying*, Ram Naidu and Carl R. Crawford
Analogic Corporation, 8 Centennial Drive, Peabody, MA 01960, USA

Received 6 September 2006

Revised 21 September 2006

Accepted 30 September 2006

Abstract. Single energy computed tomography (CT) scanners use measurements of densities to detect explosives in luggage. It is desirable to apply dual energy techniques to these CT scanners to obtain atomic number measurements to reduce false alarm rates. However, the direct application of existing dual energy techniques has practical problems, such as, approximation errors and lack of boundary constraints in dual energy decomposition, image artifacts, and x-ray spectral drifts. In this paper, we present methods to reduce these problems. The methods include constrained dual energy decomposition, adaptive scatter correction, nonlinear filtering of decomposed projections, and real-time image-based correction for x-ray spectral drifts. We demonstrate the effectiveness of the methods using simulated data and real data obtained from a commercial dual energy CT scanner.

Keywords: Computed tomography, dual energy, photoelectric effect, Compton scatter, effective atomic number, destreaking, spectral correction

1. Introduction

1.1. Motivation of dual energy CT for explosive detection

In the aftermath of September 11th, 2001, the US government mandated the deployment of certified explosive detection systems (EDS) to examine checked luggage for aircraft in the US airports by the end of 2002 [1]. As a result, there were approximately 1100 CT-based EDSs deployed in the US by the end of 2002. These deployed CT scanners produce single energy CT images of scanned baggage for explosive detection. The single energy CT images approximate the density measurements of scanned objects. The EDS detects explosives based on density, mass, and other properties of objects inside scanned luggage [2–7]. These EDSs have false alarm rates associated with detection, and the resulting falsely alarmed luggage requires labor to clear. Therefore, there is a need to reduce the false alarm rate for these CT-based EDSs in order to reduce the labor cost.

One approach to reduce the false alarm rate of these CT-based EDSs is to use dual energy techniques [4, 5, 8–10]. The dual energy techniques provide atomic number measurements of scanned objects in addition to density measurements. The atomic number measurement is usually called “effective atomic

*Corresponding author. E-mail: zying@analogic.com.

number” [11,12], which is the atomic number of a hypothetical single element that gives the same x-ray attenuation as a compound or mixture being measured. Note that in this paper we use the two terms “atomic number” and “effective atomic number” interchangeably. The atomic number measurement provides an additional dimension to the density measurement for characterizing the physical properties of scanned materials. An object’s material type can be better determined by using both its density and effective atomic number than by using the density alone [9]. For example, water and the explosive ANFO (Ammonium Nitrate and fuel oil) can have similar physical densities. However, they differ significantly in effective atomic numbers. Therefore, water and ANFO can be better discriminated from each other by a dual energy CT scanner. It has also been shown on non-CT-based x-ray systems that using both atomic number and density measurements for explosive detection can achieve a lower false alarm rate than using density measurements alone [4,5,9,10].

We have applied the dual energy techniques described in this paper to a commercial explosive detection CT scanner. This scanner has passed the TSA (Transportation Security Administration) explosive detection certification test with a lower false alarm rate than a comparable single energy CT scanner [13]. However, it is not the objective of this paper to describe how the atomic number measurement is used for automatic explosive detection, but rather to describe the details of the dual energy techniques used to obtain the atomic number measurement for explosive detection.

1.2. An overview of dual energy techniques

Interactions between x-rays with photon energy ranging from 30 KeV to 200 KeV and materials are dominated by Compton scatter and the photoelectric effect [14]. The Compton scatter and the photoelectric effect are both material and energy dependent; and each of them is modeled as the product of a material dependent coefficient and an energy dependent term, as follows:

$$\mu(x, y, z, E) = \underbrace{a_c(x, y, z)f_{\text{KN}}(E)}_{\text{Compton scatter}} + \underbrace{a_p(x, y, z)f_p(E)}_{\text{photoelectric effect}} \quad (1)$$

where (x, y, z) represent the coordinates of the material under consideration, $\mu(x, y, z, E)$ is the total x-ray attenuation, E is the incident energy, $f_p(E)$ approximates the energy dependence of the photoelectric interaction as follows:

$$f_p(E) = E^{-3} \quad (2)$$

$f_{\text{KN}}(E)$ is the Klein-Nishina cross section for Compton scatter as follows:

$$f_{\text{KN}}(\alpha) = \frac{1 + \alpha}{\alpha^2} \left[\frac{2(1 + \alpha)}{1 + 2\alpha} - \frac{1}{\alpha} \ln(1 + 2\alpha) \right] + \frac{1}{2\alpha} \ln(1 + 2\alpha) - \frac{1 + 3\alpha}{(1 + 2\alpha)^2} \quad (3)$$

and where $\alpha = E/510.975$ KeV, $a_c(x, y, z)$ is the material dependent Compton coefficient, and $a_p(x, y, z)$ is the material dependent photoelectric coefficient. The material dependent Compton and photoelectric coefficients are functions of the physical properties of scanned materials, such as the mass, density, and effective atomic number [8,14–19]. The dual energy CT scanner obtains two sets of logarithmic projections as follows:

$$P_L = -\ln \left[\int S_L(E) \exp[-A_p f_p(E) - A_c f_{\text{KN}}(E)] dE \right] + \ln \int S_L(E) dE \quad (4)$$

$$P_H = -\ln \left[\int S_H(E) \exp[-A_p f_p(E) - A_c f_{\text{KN}}(E)] dE \right] + \ln \int S_H(E) dE \quad (5)$$

where P_L and P_H are the low energy and high energy logarithmic projections, $A_c = \int a_c(x, y, z) dl(x, y, z)$ and $A_p = \int a_p(x, y, z) dl(x, y, z)$ are line integrals of the Compton coefficient, a_c , and the photoelectric coefficient, a_p , and $S_L(E)$ and $S_H(E)$ are the low energy and high energy incident x-ray spectra, respectively. In general, the dual energy projections P_L and P_H can be obtained by three categories of data acquisition mechanisms: x-ray source spectrum switching [20], filtering by transmission through different materials or thickness of materials (sandwich detectors) [21], and the use of energy resolving detectors [22]. Given the Compton and photoelectric coefficients of a material, the effective atomic number of the material can be computed using the methods described in Appendix 2.

The approaches in the literature for dual energy decomposition approximate the relationship between a set of dual energy projections, P_L and P_H , and a set of decomposed projections as polynomial functions instead of solving Eqs (4) and (5) directly [14,16,23–26]. The set of decomposed projections can be Compton projections, A_c , and photoelectric projections, A_p , or linear combinations of A_c and A_p as in different basis functions [16,23]. One approach models the dual energy projections, P_L and P_H , as polynomial functions of the decomposition projections [14]. The iterative Newton-Raphson method is then used to solve for the decomposed projections. The other approaches model the decomposed projections as polynomial functions of the dual energy projections directly [16,23,26]. Therefore the decomposed projections can be obtained given a pair of measured dual energy projections. The coefficients of these polynomial functions, which contain the information of the dual energy x-ray spectra, are obtained using various calibration methods [14–16,23–26].

1.3. Limitations of existing dual energy techniques

We applied the existing dual energy techniques to a commercial CT scanner for explosive detection as described in Appendix 1. We do not know the exact requirements for the atomic number measurement for explosive detection, in terms of the accuracy, precision, stability, and image quality. However, given our experiences in explosive detection for checked luggage screening, we believe that the following problems would have prevented us from using existing techniques directly for the purpose of explosive detection, and thereby, from meeting the explosive detection requirement set by the TSA for checked luggage screening.

1. *Approximation error*: The error due to the polynomial approximation used in the prior art methods [14,16,23–26] cannot be neglected in our application due to the large dynamic range of the photoelectric coefficients, which results from a large variety of materials in checked luggage. For example, there is over 200% approximation error when we applied the indirect approximation method of [14] to the dual energy CT scanner (Please refer to Section 3.1 for the details).
2. *Boundary constraints*: In practice, due to noise, scatter, and other sources of errors, the solution to Eqs (4) and (5) may not exist, may be numerically unstable, or may be physically meaningless (negative values of A_c or/and A_p). Simply truncating the projection values causes a saturation artifact [27].
3. *Image Artifacts*: The artifacts in the dual energy decomposed images are another issue in our application, because the image artifacts corrupt the atomic number measurements of scanned objects. The photoelectric effect is a small part of the interaction between an x-ray beam and materials at the x-ray energies at which a typical CT scanner operates. For example, the photoelectric effect only accounts for about 2% of the total x-ray attenuation for water at 80 KeV. Therefore the photoelectric image may contain artifacts due to scatter and noise [28,29]. Because the nonlinear dual energy decomposition also amplifies noise, a small amount of scatter may cause artifacts, such as a cupping effect and streaks on the photoelectric image.

Another artifact is the streak artifact. The streak artifact is caused by inconsistencies in the projection data [30]. The inconsistencies could be the result of noise, scatter, and a large dynamic range of the photoelectric coefficient. For example, the photoelectric coefficient is about $3000 \text{ KeV}^3/\text{cm}$ for plastics, and is $1,600,000 \text{ KeV}^3/\text{cm}$ for iron. Therefore, objects with a large photoelectric coefficient generate streak artifacts and affect the measurements of objects with a small photoelectric coefficient when located nearby during scanning. This is similar to the metal streaks in the single energy CT images [18,31].

4. *X-ray Spectral Drift*: All of the approaches in the literature assume that the x-ray spectra do not change from the time when a calibration is conducted to the time when a measurement scan is performed. However, we found that the x-ray spectra on our dual energy CT scanner drift over time. The drift is due to variations in thermally sensitive components of the high voltage power supply (HVPS), and the drift usually includes a short term drift on the order of hours and a long term drift on the order of days. Such drifts cause errors in the density and atomic number measurements, thus deteriorating the performance of explosive detection.

2. Algorithm description

In this section, we describe the methods used to reduce the problems encountered when applying existing dual energy techniques to the dual energy CT scanner.

2.1. Constrained decomposition method

We use the approach proposed by Kalender *et al.* [24] to decompose the dual energy projections, P_L and P_H , into Compton and photoelectric projections, A_c and A_p , by employing modeled x-ray spectra (described in Section 3). The actual spectra may be slightly different from the modeled spectra, and we describe a calibration procedure to compensate for this difference in Section 2.4. In our constrained decomposition method (CDM), we pose the dual energy decomposition problem as a constrained minimization problem. The solution, A_c and A_p , to the constrained minimization problem with any input P_L and P_H , exists, is numerically stable, and is physically meaningful. In addition, the resulting A_c and A_p are continuous functions of the dual energy projections, P_L and P_H . Thus the decomposed images do not suffer from the artifacts caused by discontinuities in A_c or A_p .

We pose the dual energy decomposition problem as the following constrained least square minimization problem:

$$(A_c, A_p) = \arg \min_{(A_c, A_p)} \underbrace{[P_L(A_c, A_p) - P_L]^2 + [P_H(A_c, A_p) - P_H]^2}_{Q(A_c, A_p)} \quad (6)$$

subject to the constraints:

$$A_c \geq 0 \quad A_p \geq 0 \quad (7)$$

where P_L and P_H are measured dual energy projections, $P_L(A_c, A_p)$ and $P_H(A_c, A_p)$ are the modeled dual energy projections as described in Eqs (4) and (5) respectively, and $Q(A_c, A_p)$ is the cost function. Note that (A_c, A_p) denotes a pair of Compton projection, A_c , and photoelectric projection, A_p , to be optimized. The notation “arg” means that the left hand part of the equation is replaced with the values of (A_c, A_p) that minimize the right hand side of the equation.

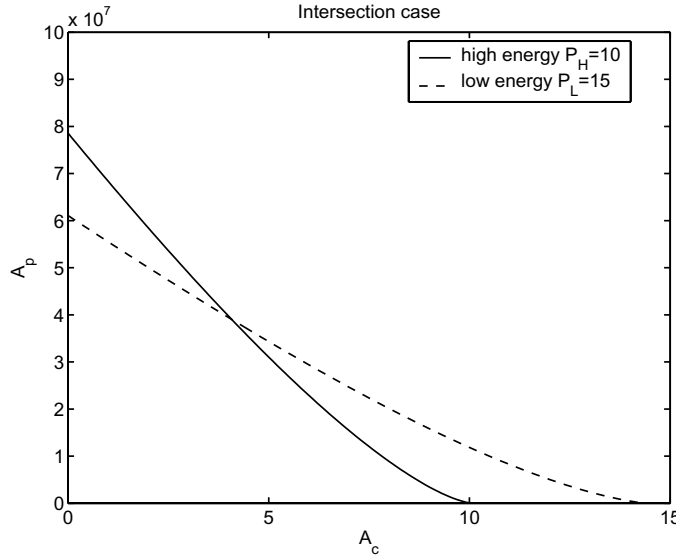


Fig. 1. Two isotransmission curves intersect in the first quadrant.

The above constrained optimization problem can be solved using Lagrange multiplier methods [32]. However, we describe the following optimization procedure, which takes advantage of the special structure of the cost function $Q(A_c, A_p)$. The minimization problem can be broken into two sub-cases and solved individually.

The solution to the above minimization problem is described intuitively using isotransmission curves [27]. An isotransmission curve is a function that describes A_p in terms of A_c , given a projection value, P_L , or P_H , with x-ray spectrum $S_L(E)$, or $S_H(E)$. Therefore, dual energy projections, P_L and P_H , correspond to two isotransmission curves in the (A_c, A_p) space. When these two isotransmission curves intersect in the first quadrant (including the two axes), there exist $A_c \geq 0$ and $A_p \geq 0$ corresponding to the input projections, P_L and P_H , that results in $Q(A_c, A_p) = 0$. This case is illustrated in Fig. 1. The two-dimensional Newton-Raphson method [33] is used to obtain the solution iteratively by using the Jacobian of the Eqs (4) and (5).

When the isotransmission curves corresponding to the input projections, P_L and P_H , do not intersect in the first quadrant, there is no pair (A_c, A_p) , that yields $Q(A_c, A_p) = 0$. This is determined by the convergence of the A_c and A_p within the first quadrant by using the two-dimensional Newton-Raphson method. Such cases are illustrated in Fig. 2. In these cases, we force either A_c or A_p to be zero; i.e. when the two isotransmission curves do not intersect in the first quadrant, we require that the solution be in the form of either $(A_c \geq 0, A_p = 0)$ or $(A_c = 0, A_p \geq 0)$, minimizing the least square error $Q(A_c, A_p)$.

The minimization with the solution in the format of either $(A_c \geq 0, A_p = 0)$ or $(A_c = 0, A_p \geq 0)$ is solved iteratively using the Newton-Gauss method [33], a gradient descent algorithm using the inverse of second order derivatives as the step size. Hence, two possible solutions are obtained in the format of $(A_c \geq 0, A_p = 0)$ or $(A_c = 0, A_p \geq 0)$. The final solution is chosen to be the one which yields smaller least square error. The above iterative algorithm usually converges to an error, which is the difference between two consecutive solutions, of 10^{-6} in less than 10 iterations.

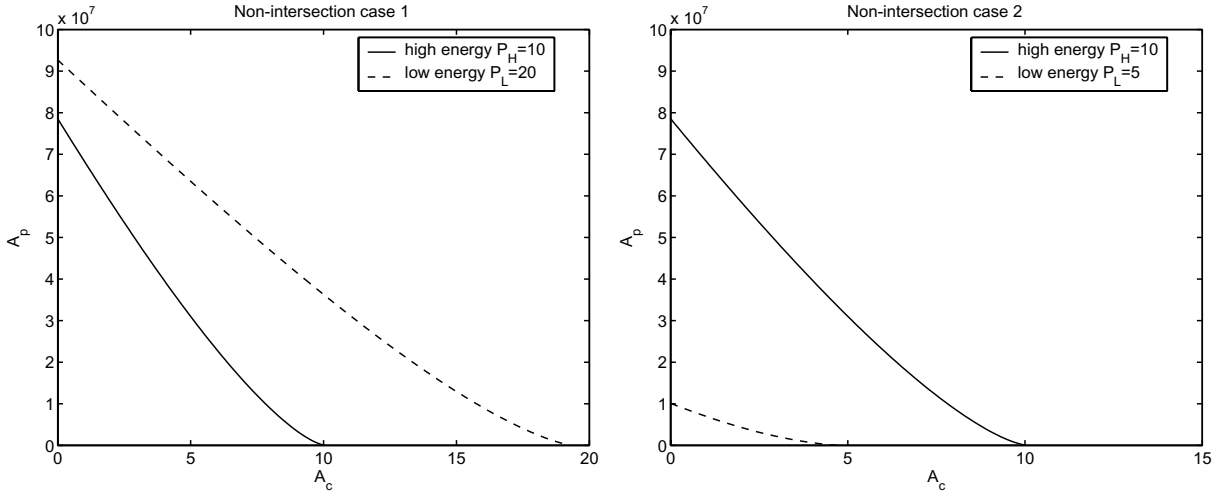


Fig. 2. Two isotransmission curves do not intersect in the first quadrant.

2.2. Adaptive scatter correction

There is a large body of literature for estimating and correcting scatter for medical CT applications [34–42], and we are not aware of any literature dealing with scatter in the application of luggage CT scanning. The methods developed for medical CT application assume an elliptical shape of a scanned object. Also note that the dynamic range of density and atomic number in a medical CT scanner is from air to bone, while in our luggage CT scanner, the dynamic range is much bigger, i.e. from air to metal objects.

It is our belief that Glover’s scatter correction [34] is more general and can be extended for our luggage CT application. Thus, our adaptive scatter correction algorithm is an extension of Glover’s scatter correction algorithm. Glover corrects scatter in the projection space (logarithm space, or attenuation space) using the first order approximation as follows:

$$P_{\text{corr}} = P_{\text{meas}} + \underbrace{\alpha \exp(P_{\text{meas}})}_{P_{\text{scatter}}} \quad (8)$$

where P_{corr} is the scatter corrected projection, P_{meas} is the measured projection, P_{scatter} is the equivalent projection due to the scatter, and α is a nonnegative constant, representing the ratio of the scatter intensity to the air intensity, which is the intensity received by the detectors in the absence of any object in the x-ray path.

The scatter correction algorithm described in Eq. (8) assumes that scatter only depends on the projection value of a single detector. However, because scatter is a spatially correlated process [35,40,42], we found that Glover’s algorithm does not reduce scatter artifacts in the decomposed image. Therefore, we extend Glover’s algorithm to incorporate the spatial dependence by making α in Eq. (8) detector dependent.

We use a low-pass filter, denoted as $h(n)$, to incorporate the spatial correlation into the scatter estimation. Furthermore, the spatial support (or size) of the low-pass filter is also adaptive to account for the size and density of the objects. For example, when there is a large dense object in the scanning field, there is more scatter; therefore the support of the low-pass filter is large. Otherwise, the support of the low-pass filter is small.

The input projection is defined in a three-dimensional space: projection angle, detector row, and detector column. For the simplicity of exposition, we describe our adaptation scheme along one row

of detectors. Denoting the detector index along one row as s ($0 \leq s < S$), and input dual energy projections as $P'_L(s)$ and $P'_H(s)$, we first estimate the low-pass filter length W . Note that the low-pass filter length is fixed for one entire detector row, but varies from row to row and from projection angle to projection angle. The filter length, W , is an indicator of the size of scanned objects that are dense enough to generate scatter. Therefore we use projection data for estimating the filter length. Both the high and low energy projections can be used for estimating the filter length, W , and we only show the estimation based on the high energy projections as follows,

$$W = \left\lfloor \max_s C(s) \right\rfloor \quad (9)$$

where $\lfloor x \rfloor$ is the largest integer no greater than x , and

$$C(s) = \sum_{s'=\max(s,0)}^{\min(S-1,s+W_0)} u \left(P'_H \left(s' - \left\lfloor \frac{W_0}{2} \right\rfloor \right) - P_0 \right) \quad (10)$$

where W_0 is an initial guess of the low-pass filter length, P_0 is a threshold to remove the influence of objects which are not denser than P_0 , and $u(\cdot)$ is a step function as follows:

$$u(x) = \begin{cases} 1, & x \geq 0 \\ 0, & x < 0 \end{cases} \quad (11)$$

Given the estimated low-pass filter size W , we use the low-pass filtered projections as the adaptive scatter coefficient α as in Eq. (8). A scatter profile is assumed to be the same for both high and low energy projections, therefore the estimated filter length, W , from the high energy projections is used for calculating adaptive scatter coefficients of both high and low projections. Let $h(n)$ ($0 \leq n < W$, $\sum_{n=0}^{W-1} h(n) = 1$) be the low-pass filter with the estimated length, W . We then have the following adaptive $\alpha_L(s)$ for low energy projections and $\alpha_H(s)$ for high energy projections:

$$\alpha_L(s) = \sigma_L \sum_{n=-\lfloor W/2 \rfloor}^{\lfloor (W-1)/2 \rfloor} P'_L(s+n)h(n + \lfloor W/2 \rfloor) \quad (12)$$

$$\alpha_H(s) = \sigma_H \sum_{n=-\lfloor W/2 \rfloor}^{\lfloor (W-1)/2 \rfloor} P'_H(s+n)h(n + \lfloor W/2 \rfloor) \quad (13)$$

where σ_L and σ_H are constants, which are empirically determined. Zero-padding is used for the boundaries ($s < 0$ and $s \geq W$) of $P'_L(s)$ and $P'_H(s)$.

The scatter corrected dual energy projections, $P_L(s)$ and $P_H(s)$, are then computed as follows:

$$P_L(s) = P'_L(s) + \alpha_L(s) \exp(P'_L(s)) \quad (14)$$

$$P_H(s) = P'_H(s) + \alpha_H(s) \exp(P'_H(s)) \quad (15)$$

The adaptive scatter correction algorithm described above adapts the scatter coefficients, $\alpha_L(s)$ and $\alpha_H(s)$, to the size and density of the scanned objects. When the object is large, the support of the low-pass filter, W , is large; when the scanned object is dense, the scatter coefficients are large.

The parameters such as P_0 , W_0 , σ_L , and σ_H were experimentally determined to provide improved image quality over scanned explosives in different configurations.

Note that the above adaption scheme is independent in each row of a 2D detector array and the filter size in each row remains constant; these are due to constraints of computing power. It can be straightforwardly extended to take 2D spatial correlation of scatter into account and adapt the filter size along each row.

2.3. Destreaking

The streak artifact is caused by inconsistencies in the projection data [30]. The inconsistencies could be the result of noise, scatter, a large dynamic range of the photoelectric coefficient. In order to reduce the inconsistencies, we apply a nonlinear filter to the decomposed photoelectric projection data. The projection data is three-dimensional: detector row with index r , detector column with index c , and projection angle with index v . The input photoelectric projection is denoted as $A_p(r, c, v)$, and the filtered photoelectric projection is denoted as A'_p , which is computed as follows:

$$A'_p(r, c, v) = \begin{cases} \bar{A}_p(r, c, v) + \sigma(r, c, v)T, & A_p(r, c, v) - \bar{A}_p(r, c, v) > \sigma(r, c, v)T \\ \bar{A}_p(r, c, v) - \sigma(r, c, v)T, & A_p(r, c, v) - \bar{A}_p(r, c, v) < -\sigma(r, c, v)T \\ A_p(r, c, v), & |A_p(r, c, v) - \bar{A}_p(r, c, v)| \leq \sigma(r, c, v)T \end{cases} \quad (16)$$

where T is a constant, and

$$\bar{A}_p(r, c, v) = \frac{1}{N} \sum_{(r', c', v') \in C(r, c, v)} A_p(r', c', v') \quad (17)$$

$$\sigma(r, c, v) = \sqrt{\frac{1}{N} \sum_{(r', c', v') \in C(r, c, v)} [A_p(r', c', v') - \bar{A}_p(r, c, v)]^2} \quad (18)$$

where $C(r, c, v)$ is a set of predefined neighborhood samples of (r, c, v) . In our implementation, we use the following six-neighbor scheme,

$$C(r, c, v) = \{(r', c', v') : |r' - r| + |c' - c| + |v' - v| = 1\} \quad (19)$$

In the above nonlinear filtering, we retain the photoelectric projection value that is consistent with its neighbors, and replace the inconsistent projections with the allowed limits derived from its neighbors. We use the range derived from the second order statistics, namely, the mean and the standard deviation, of the neighbors as the consistency criterion. This nonlinear filtering criterion adapts to the distribution of the neighbors: when the standard deviation of the neighbors is large, the consistency range increases; otherwise, it decreases. Therefore, instead of setting one uniform threshold for all the projection data, we allow the filter to adapt to the statistics of the data. Note that the filtered projection is a continuous function in terms of the input projection.

2.4. Spectral correction

The dual energy CT scanner produces images of measurements of CT numbers, denoted as H , and atomic numbers, denoted as Z of scanned objects. The values of H and Z are obtained by processing dual energy projections measured with two x-ray spectra, and using the non-linear decomposition algorithm described in Section 2.1. The decomposition is performed using fixed x-ray spectra for all the scanners. However, different scanners have different spectra due to variations in beamline components, such as x-ray tubes, filtration materials, and detectors. The spectra on each scanner also vary with time due to voltage drifts in the HVPS. As a result, H and Z vary along time on an individual scanner, and vary from scanner to scanner as well. In this section, we describe our method for correcting H and Z for these spectral variations.

X-ray spectra on each scanner are tracked and compensated in real-time using reference materials described below. To simplify the notation, we use vector and matrix representation for description. Let $\mathbf{x} = [H, Z]^T$ be the vector containing the CT number and the atomic number. We use the following linear model to correct the spectral variations across scanners:

$$\mathbf{x}' = \mathbf{x}_0 + \mathbf{S}(\mathbf{x} - \tilde{\mathbf{x}}_0) \quad (20)$$

where \mathbf{x}_0 contains the nominal (actual) CT number and atomic number of the 0th reference material, \mathbf{x} contains the measured CT number and atomic number for a scanned material, $\tilde{\mathbf{x}}_0$ contains the expected CT number and atomic number of the 0th reference material when hypothetically measured at the same x-ray spectra for generating \mathbf{x} of the scanned material, \mathbf{x}' contains the spectrally corrected CT number and atomic number, and \mathbf{S} is a 2×2 parameter matrix as follows:

$$\mathbf{S} = \begin{bmatrix} s_{hh} & s_{hz} \\ s_{zh} & s_{zz} \end{bmatrix} \quad (21)$$

The parameters can be computed by solving the following $2(N - 1)$ linear equations:

$$\mathbf{x}_i = \mathbf{x}_0 + \mathbf{S}(\tilde{\mathbf{x}}_i - \tilde{\mathbf{x}}_0), \quad i = 1, \dots, N - 1 \quad (22)$$

where \mathbf{x}_i contains the i^{th} reference material's nominal CT number and atomic number, and $\tilde{\mathbf{x}}_i$ contains the i^{th} reference material's expected CT number and atomic number when hypothetically measured at the same x-ray spectra used to generate \mathbf{x} (in Eq. (20)) of the scanned material.

Since there are four parameters in each parameter matrix \mathbf{S}_i , at least four system equations ($2(N - 1) \geq 4$) are required to obtain a unique solution. Therefore, at least three materials ($N \geq 3$) are needed for calibration.

We use a copper filter mounted over some detectors on the detector array to detect and track changes of x-ray spectra on each scanner. Let I_a^l and I_a^h be the low energy and high energy x-ray intensities received by the detectors without the copper filter, respectively, and I_c^l and I_c^h be the low energy and high energy x-ray intensities received by the detectors shielded by the copper filter, respectively. We compute the low energy copper ratio, denoted as R^l , and high energy copper ratio, denoted as R^h , as follows:

$$R^l = \frac{I_a^l}{I_c^l}, \quad R^h = \frac{I_a^h}{I_c^h} \quad (23)$$

Let vector $\mathbf{r} = [R^l, R^h]^T$ denote the vector containing low energy and high energy copper ratios for the convenience of exposition.

The expected value of $\tilde{\mathbf{x}}_i$ ($i = 0, \dots, N - 1$) of the i^{th} reference material is computed by using the following linear model:

$$\tilde{\mathbf{x}}_i = \hat{\mathbf{x}}_i^0 + \mathbf{M}_i (\mathbf{r} - \mathbf{r}_0) \quad (24)$$

where $\hat{\mathbf{x}}_i^0$ contains the 0^{th} measured CT number and atomic number of the i^{th} material during a calibration, \mathbf{r} contains the copper ratios corresponding to \mathbf{x} , \mathbf{r}_0 contains the copper ratios corresponding to $\hat{\mathbf{x}}_i^0$, and \mathbf{M}_i is a 2×2 parameter matrix as follows:

$$\mathbf{M}_i = \begin{bmatrix} m_{hh}^i & m_{hl}^i \\ m_{lh}^i & m_{ll}^i \end{bmatrix} \quad (25)$$

The parameters in the matrix \mathbf{M}_i ($i = 0, \dots, N - 1$) are obtained by the following calibration.

The calibration involves scanning N materials at L different spectra. After the calibration is performed, the calibration parameters \mathbf{M}_i ($i = 0, \dots, N - 1$) are stored in the reconstruction computer and are used for the spectral correction as described above.

The first (0^{th}) measurement is performed at the spectra corresponding to the scanner's nominal operating point. The rest of the measurements are taken by perturbing the x-ray spectra around the nominal operating point to simulate the HVPS drift. N materials are contained in a case, so that they can be measured simultaneously. For the j^{th} measurement, the measured CT number and atomic number $\hat{\mathbf{x}}_i^j$ ($i = 0, \dots, N - 1$) and the corresponding copper ratios \mathbf{r}_j are recorded. The parameters \mathbf{M}_i are obtained by solving the following $2(L - 1)$ system equations:

$$\hat{\mathbf{x}}_i^j = \hat{\mathbf{x}}_i^0 + \mathbf{M}_i (\mathbf{r}_j - \mathbf{r}_0), \quad j = 1, \dots, L - 1 \quad (26)$$

Since there are four parameters in each parameter matrix \mathbf{M}_i , at least four system equations ($2(L - 1) \geq 4$) are required to obtain a unique solution. Therefore, at least three measurements ($L \geq 3$) are needed for calibration.

The spectral correction algorithm is performed on reconstructed images in real-time on a quad-CPU reconstruction computer. The copper ratios are updated every rotation to track the change of the x-ray spectra. Every reconstructed CT image and every reconstructed Z image are corrected in a pixel-by-pixel basis with the latest copper ratios.

3. Experiments and results

In this section, we demonstrate the effectiveness of our dual energy techniques using simulated and real data. We compare our constrained decomposition method (CDM) with methods from the literature with respect to decomposition approximation errors and errors due to boundary conditions. We also show the image quality improvement produced by the adaptive scatter correction algorithm and destreaking algorithm using real data obtained from the dual energy CT scanner. Finally, we demonstrate the effectiveness of the spectral correction algorithm for compensating the spectral drift of the dual energy CT scanners.

3.1. Approximation error

In this experiment, we evaluated the approximation error in the decomposition using our CDM method as described in Section 2.1 and the indirect polynomial approximation method [14], denoted here as

the AM method. We compared the results of our CDM method with the AM method, because the AM method is a representative method of the polynomial approximation methods in the literature. We used simulation in our experiment so that no other sources of errors affected experimental results.

We used the dual energy x-ray spectra generated according to Appendix 3 for the simulation. The calibration was performed as follows to obtain the 16 polynomial coefficients of Eqs (12) and (13) as described in [14]. We generated 14,400 candidate calibration points: A_c ranges from 0.1 to 12.0 with a step size of 0.1; $A_p^{\frac{1}{3}}$ ranges from 3 KeV to 360 KeV with a step size of 3 KeV. For each pair, A_c and A_p , we generated the corresponding pair, P_L and P_H using Eqs (4) and (5). Among these 14,400 candidate calibration points, we used those points with both $P_L \leq 12$ and $P_H \leq 12$ as calibration points. This resulted in total of 8,997 calibration points for obtaining 16 polynomial coefficients of the AM method. The polynomial coefficients were obtained by a minimum mean square error method through solving these 8,997 overdetermined linear system equations. In order to avoid the numerical instability in solving for the polynomial coefficients, we scaled the maximum value of A_p down to 10 KeV^3 .

To test the decomposition algorithm, we generated dual energy projections using the dual energy CT scanner geometry as described in Appendix 1 for a 20 cm diameter cylindrical water phantom centered at the isocenter of the scanner. The projections were generated in an axial scan mode. The Compton coefficient and the photoelectric coefficient for water used in the experiment were 0.163 cm^{-1} and $4,645 \text{ KeV}^3/\text{cm}$, respectively [27].

We used the two-dimensional Newton-Raphson method to iteratively solve for A_c and A_p given the 16 polynomial coefficients of the AM method. The stopping criterion used in the experiment was that the sum of the absolute change of A_c and A_p between two consecutive iterations was less than 10^{-6} . We used the maximum projection values corresponding to the detector number 126 (detectors are numbered from 1) for computing the percentage errors $E\% = \frac{A_{\text{est}} - A_{\text{true}}}{A_{\text{true}}} \times 100\%$, where A_{est} is the estimated value of the true A_{true} . The errors of A_c and A_p of the AM method are 1.50% and 238.25%, respectively. The corresponding errors of our method are 0.00008% and 0.0002%, respectively. Note that the errors in the CDM method are due to the numerical error, while the errors in the AM method are dominantly due to the approximation error. Also note that the much larger error of A_p is due to the fact that A_p is more sensitive to any source of errors. The negative value of A_p from the AM method resulted in meaningless values of physical properties of the scanned objects, such as negative atomic numbers. Therefore, such a large approximation error prevents us from applying these existing polynomial approximating methods directly to our application.

3.2. Boundary constraints

We used simulated data to demonstrate the performance improvement of our constrained decomposition method over the truncation method as suggested in [27] for handling the boundary conditions. The truncation method was implemented with our best guess from [27].

We first randomly generated A_c and A_p pairs, of which A_c was uniformly distributed between 0 and 12 and A_p was uniformly distributed between 0 and 4.5×10^7 . For each pair, A_c and A_p , we computed the corresponding dual energy projection pair, P_L and P_H , according to Eqs (4) and (5).

We then added photon noise, which was modeled as a Poisson process [43,44], to each pair of dual energy projections as follows:

$$\tilde{P}_L = \ln n_{L0} - \ln (g(n_{L0} \exp(-P_L))) \quad (27)$$

$$\tilde{P}_H = \ln n_{H0} - \ln (g(n_{H0} \exp(-P_H))) \quad (28)$$

where \tilde{P}_L and \tilde{P}_H are the noise corrupted low and high energy projections, n_{L0} and n_{H0} are the number of photons of the low and high energy incident x-rays, and $g(\lambda)$ is a random point process according to the Poisson distribution with mean λ . In this experiment, $n_{L0} = 5 \times 10^5$, and $n_{H0} = 1 \times 10^6$.

In the truncation method, we used the two-dimensional Newton-Raphson iterative method to solve for a pair of decomposed projections, A_c and A_p , given a pair of noise corrupted \tilde{P}_L and \tilde{P}_H . We used the following criterion for truncation:

$$\tilde{A}_c = \begin{cases} 0, & A_c < 0 & \text{(a)} \\ 0, & A_c = \text{NaN} & \text{(b)} \\ A_c, & \text{otherwise} \end{cases} \quad \tilde{A}_p = \begin{cases} 0, & A_p < 0 & \text{(c)} \\ 0, & A_p = \text{NaN} & \text{(d)} \\ A_p, & \text{otherwise} \end{cases} \quad (29)$$

where \tilde{A}_c and \tilde{A}_p are the truncated decomposed projections, NaN denotes Not a Number as defined in the IEEE standard 754 for floating point numbers. Note that the truncation is only applied when one or more of (a), (b), (c), (d) conditions occurs. Among all generated pairs, (A_c, A_p) , there were 100,000 truncation cases.

We also used our constrained decomposition method to decompose the same 100,000 noise corrupted dual energy projections into decomposed projections. Our constrained decomposition method did not yield any NaN solutions.

We define the error, E , as the follows for comparing the performance between our constrained decomposition method and the truncation method:

$$E = \left[\frac{\tilde{A}_c - A_c}{A_c} \right]^2 + \left[\frac{\tilde{A}_p - A_p}{A_p} \right]^2 \quad (30)$$

where A_c and A_p are the uniformly generated true Compton projection and the true photoelectric projection respectively, and \tilde{A}_c and \tilde{A}_p are the decomposed results of the noise corrupted dual energy projections using either the truncation method or our constrained decomposition method. The truncation method yielded an error of 6355 and our constrained decomposition method had an error of 3119. Our constrained decomposition method reduced the error caused by the truncation method during the decomposition by about 50%, demonstrating the robustness of our method to noise.

3.3. Scatter correction

We tested our adaptive scatter correction algorithm over numerous images obtained from the scanner, and we show a representative example of these tested images below.

Figure 3 shows the Z images of a cross section of a Nylon cylinder. Figure 3(a) shows the Z image without scatter correction, and Fig. 3(b) shows the Z image with scatter correction. In this case, the image without scatter correction shows both the amplified noise effect introduced during the dual energy decomposition procedure and cupping artifacts.

The above images qualitatively demonstrate that our algorithm is effective in reducing the cupping artifacts and noise. In order to quantitatively measure the improvements of the image quality of the effective-atomic-number image from our scatter correction algorithm, we define the following measures.

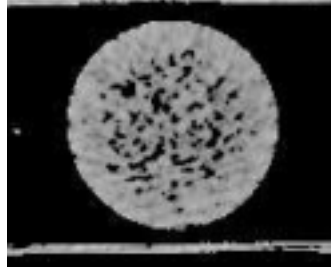
1. Mean of the effective atomic number Z_{mean} from an object;
2. Cupping ratio R is defined as follows,

$$R = \frac{Z_{\text{bon}} - Z_{\text{cen}}}{Z_{\text{bon}}} \times 100\% \quad (31)$$

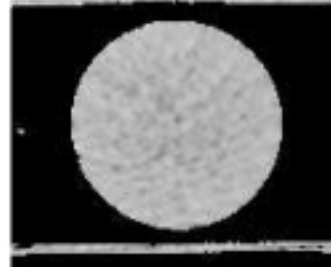
Table 1

Quantitative comparison of the effective-atomic-number images before and after scatter correction. Note that the true effective atomic numbers of the two explosives are not known (as denoted by NA)

| Materials | mean Z | | | cupping ratio R | | SNR (dB) | |
|-------------|----------|--------|-------|-------------------|-------|------------|-------|
| | true | before | after | before | after | before | after |
| Aluminum | 13 | 11.5 | 13.1 | 47% | 31 % | 15.0 | 18.0 |
| Nylon | 6.33 | 3.02 | 7.13 | 23% | 7% | 1.8 | 19.1 |
| Explosive 1 | NA | 6.55 | 9.19 | 37% | 11% | 9.5 | 14.5 |
| Explosive 2 | NA | 7.20 | 7.40 | 27% | 24% | 14.1 | 14.7 |



(a) without scatter correction



(b) with scatter correction

Fig. 3. Z images (atomic number multiplied by 100) of a cross section of a Nylon cylinder, window = 1400, level = 700.

where Z_{cen} is the effective atomic number at the center of an object, and Z_{bon} is the effective atomic number at the boundary of an object. In this definition, image without cupping artifact has the cupping ratio of 0.

3. SNR of the effective-atomic-number image is defined as follows,

$$SNR = 20 \log_{10} \frac{Z_{\text{mean}}}{Z_{\sigma}} \quad (32)$$

where Z_{mean} is the mean of the effective atomic number of an object, and Z_{σ} is the standard deviation of the effective atomic number of the corresponding object.

Table 1 lists comparison of four scanned materials in terms of mean atomic number, cupping ratio, and SNR. For all the listed materials, the scatter correction algorithm improves the SNR and reduces the cupping ratio, indicating the effectiveness of our algorithm.

3.4. Destreaking

We also tested our destreaking algorithm over numerous images obtained from the scanner, and a representative example of the tested images is shown in Fig. 4. The images with destreaking have much less streaks than the images without destreaking. Furthermore, the folded sheet explosive simulant is not blurred by the destreaking algorithm.

In order to obtain the quantitative measurements in terms of the quality improvements in Z images, we calculated the quantitative measurements such as mean of the effective atomic number and SNR, as defined in Section 3.3, for different materials. Table 2 lists the mean of effective atomic number and SNR before and after our destreaking algorithm. Our algorithm improves all these quantitative measurements for the Z image, indicating the effectiveness of our destreaking algorithm. Note that the SNR of low Z

Table 2

Quantitative comparison of the Z images before and after destreaking. Note that the true effective atomic numbers of the two explosives are not known

| Materials | mean Z | | | SNR (dB) | |
|-------------|----------|--------|-------|------------|-------|
| | true | before | after | before | after |
| Nylon | 6.33 | 4.83 | 7.13 | 2.7 | 19.1 |
| Explosive A | NA | 8.92 | 9.19 | 10.5 | 14.5 |
| Explosive B | NA | 7.26 | 7.40 | 10.7 | 14.7 |
| Aluminum | 13 | 12.9 | 13.1 | 17.2 | 18.0 |

Table 3

Nominal atomic numbers and nominal CT numbers for the three reference materials used in the spectral calibration

| Material reference # (i) | 0 | 1 | 2 |
|--------------------------|-------|--------|-------|
| Material | Nylon | TEFLON | PVC |
| Nominal atomic number | 6.62 | 8.21 | 14.53 |
| Nominal CT number | 1163 | 2016 | 1838 |

Table 4

DC and AC settings of the HVPS for the spectral calibration

| Measurement # (j) | 0 | 1 | 2 | 3 | 4 |
|-------------------|-----|-----|-----|-----|-----|
| DC voltage (KV) | 140 | 140 | 140 | 135 | 130 |
| AC voltage (KV) | 40 | 38 | 36 | 40 | 40 |

materials such as Nylon has more improvements than high Z materials such as Aluminum, this is due to the fact that the photoelectric effect is much smaller in low Z materials than in high Z materials.

3.5. Spectral correction

In this experiment, we first describe our spectral calibration procedure for the dual energy scanner. We used an image quality phantom (IQP) for the calibration [45]. The IQP contains three bulk materials: a Nylon cylinder, a PVC cylinder, and a TEFLON cylinder, and other objects for measuring the image quality of the scanner. We used these three bulk materials as our reference materials, which are described in Section 2.4. The Nylon cylinder was used as the 0th reference material, the TEFLON cylinder was used as the 1st reference material, and the PVC cylinder was used as the 2nd reference material. The nominal atomic numbers and nominal CT numbers of these materials are listed in Table 3.

As described in Section 2.4, at least three measurements are needed during the calibration with different x-ray spectra. We used five measurements to obtain the i^{th} material calibration parameters \mathbf{M}_i with $i = 0, 1, 2$. We changed the DC voltage and the AC voltage to simulate the HVPS drift, and the resulting x-ray spectra drifted accordingly. The DC and AC settings for the calibration are shown in Table 4.

For each DC and AC setting, we reconstructed the corresponding CT image and atomic number image, and measured the CT numbers and atomic numbers of the three materials. We also recorded the corresponding copper ratios for each scan. We then solved the system equations described in Eq. (26) for the calibration parameters, \mathbf{M}_i , with $i = 0, 1, 2$.

We also used different DC voltages and AC voltages to test the effectiveness of our spectral correction algorithm. The atomic numbers of the three materials: Nylon, TEFLON, and PVC before and after

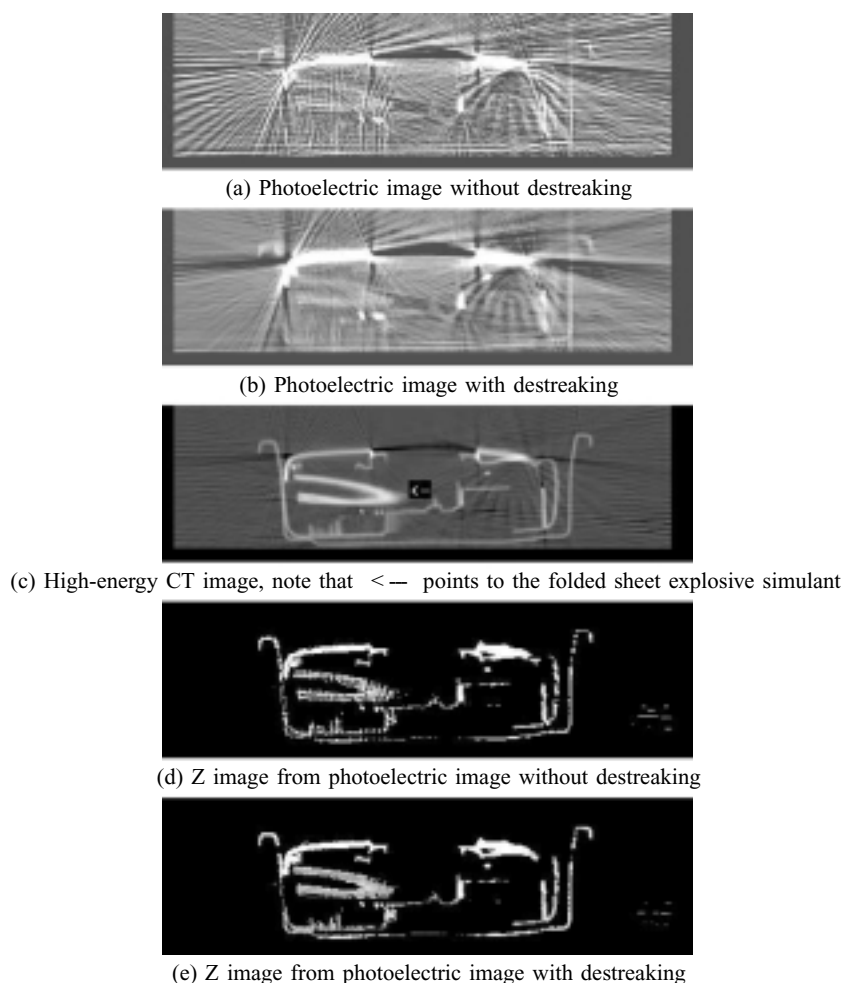


Fig. 4. A folded sheet explosive (simulant) concealed inside a radio cassette player. (a) the photoelectric image without destreaking, window = 1000, level = 400; (b) the photoelectric image with destreaking, window = 1000, level = 400; (c) high-energy CT image, window = 2000, level = 1000; (d) The Z image computed using the photoelectric image without destreaking and the high-energy CT image, window = 1000, level = 600; (e) The Z image computed using the destreaked photoelectric image and the high-energy CT image, window = 1000, level = 600; Note that the value in the photoelectric image is the measured photoelectric coefficient multiplied by 10^{-5} ; the value in the Z image is the measured effective atomic number multiplied by 100.

the correction are shown in Table 5. The spectral correction reduces the variation range of the atomic number from 1.83 to 0.26 for Nylon, from 2.09 to 0.21 for TEFLON, and from 2.60 to 0.25 for PVC. The reduction of the variation range of the atomic number measurement is about 90%.

We also performed the same test for five scanners. The results are summarized in Table 6. For each of the three materials, we show the mid-range value and the range of the atomic numbers before and after the spectral correction. The mid-range value is the average of the maximum and minimum values, and the range is the difference between the maximum and minimum values. The spectral correction yields about 90% variation range reduction on all five scanners, with the mid-range values varying within 0.11 atomic number units for all three materials.

These experimental results demonstrate that our spectral correction algorithm is effective in compen-

Table 5

Testing results of the spectral correction on one scanner. This table lists the effective atomic numbers of different materials before and after the spectral correction. The spectral correction reduces the variation range of the atomic number measurements from 1.83 to 0.26 for Nylon, from 2.09 to 0.21 for TEFLON, and from 2.60 to 0.25 for PVC. The reduction of the variation range of the atomic number measurements is about 90%

| Test # | DC (KV) | AC (KV) | Nylon | | TEFLON | | PVC | |
|--------|---------|---------|--------|-------|--------|-------|--------|-------|
| | | | before | after | before | after | before | after |
| 1 | 140 | 40.0 | 6.69 | 6.64 | 8.13 | 8.21 | 14.33 | 14.53 |
| 2 | 140 | 38.0 | 6.17 | 6.62 | 7.68 | 8.23 | 13.87 | 14.55 |
| 3 | 135 | 40.0 | 6.96 | 6.63 | 8.50 | 8.23 | 14.85 | 14.55 |
| 4 | 127 | 40.0 | 7.52 | 6.53 | 9.18 | 8.13 | 15.80 | 14.43 |
| 5 | 130 | 40.0 | 7.32 | 6.62 | 8.93 | 8.22 | 15.45 | 14.53 |
| 6 | 132 | 40.0 | 7.19 | 6.64 | 8.77 | 8.24 | 15.20 | 14.53 |
| 7 | 137 | 40.0 | 6.86 | 6.64 | 8.37 | 8.24 | 14.67 | 14.57 |
| 8 | 125 | 40.0 | 7.57 | 6.40 | 9.31 | 8.03 | 15.99 | 14.32 |
| 9 | 140 | 36.0 | 5.74 | 6.63 | 7.21 | 8.19 | 13.40 | 14.52 |
| 10 | 140 | 37.2 | 6.03 | 6.65 | 7.51 | 8.22 | 13.69 | 14.55 |
| 11 | 140 | 38.8 | 6.12 | 6.39 | 7.72 | 8.11 | 13.97 | 14.49 |
| 12 | 140 | 39.6 | 6.45 | 6.55 | 7.91 | 8.15 | 14.10 | 14.50 |
| 13 | 142 | 39.2 | 6.29 | 6.55 | 7.74 | 8.15 | 13.89 | 14.49 |
| 14 | 143 | 38.8 | 6.18 | 6.53 | 7.59 | 8.11 | 13.72 | 14.45 |

Table 6

Testing results of the spectral correction on five scanners. This table shows the mid-range values and variation ranges of the atomic number measurements of different materials scanned on different scanners. It shows that the spectral correction reduces the variation range of the atomic number measurements for about 90% on all five tested scanners

| scanner # | | | 1 | 2 | 3 | 4 | 5 |
|-----------|-----------|--------|-------|-------|-------|-------|-------|
| Nylon | mid-range | before | 6.65 | 6.36 | 6.63 | 6.22 | 6.73 |
| | | after | 6.52 | 6.62 | 6.63 | 6.60 | 6.63 |
| | range | before | 1.83 | 1.93 | 2.06 | 2.88 | 2.04 |
| | | after | 0.26 | 0.29 | 0.52 | 0.47 | 0.47 |
| TEFLON | mid-range | before | 8.26 | 8.16 | 8.27 | 7.90 | 8.30 |
| | | after | 8.14 | 8.25 | 8.21 | 8.20 | 8.23 |
| | range | before | 2.09 | 1.88 | 2.29 | 2.68 | 2.25 |
| | | after | 0.21 | 0.30 | 0.43 | 0.28 | 0.33 |
| PVC | mid-range | before | 14.70 | 14.51 | 14.62 | 14.36 | 14.65 |
| | | after | 14.44 | 14.55 | 14.51 | 14.53 | 14.55 |
| | range | before | 2.60 | 2.40 | 2.68 | 2.87 | 2.71 |
| | | after | 0.25 | 0.21 | 0.29 | 0.17 | 0.17 |

sating the atomic number measurement for the x-ray spectral drift on individual dual energy CT scanners and for the beamline components variation across scanners.

4. Discussion

In this paper, we have described our dual energy techniques, which have been applied to a commercial dual energy CT scanner for explosive detection in checked luggage. Although the dual energy techniques presented in this paper are developed particularly for our CT scanner, we believe these techniques can be extended to other types of scanners, such as dual energy CT scanners using sandwich detectors.

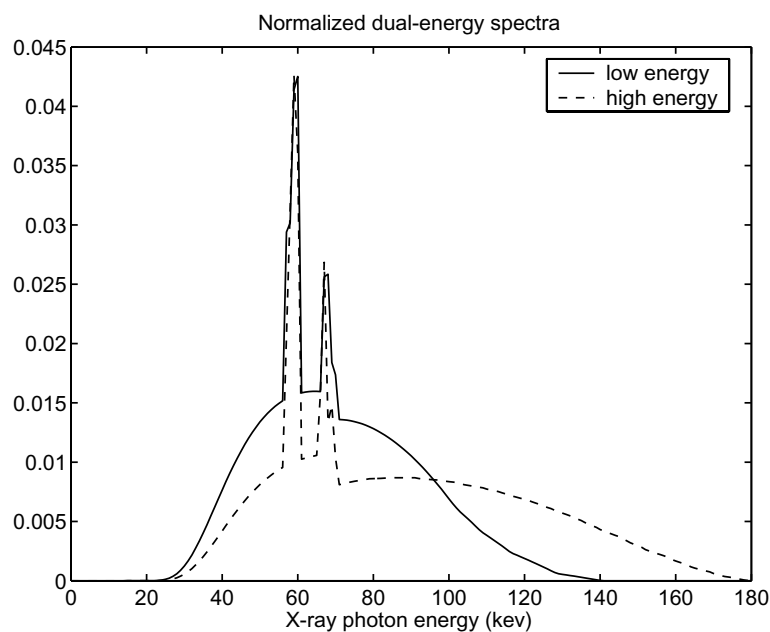


Fig. 5. X-ray spectra used in the dual energy decomposition for all the scanners.

The constrained decomposition method does not depend on the particular scanner geometry or data acquisition method of dual energy projections. The adaptive scatter correction algorithm uses projection data itself to estimate scatter. The destreaking algorithm is also a data dependent process for removing outliers, which represent inconsistencies in the projection data. Both algorithms do not require any additional sensors or mechanisms, therefore, they can be extended and applied to other types of scanners directly. The spectral correction algorithm requires a copper filter mounted over some detectors on the detector array. The same algorithm can also be applied to the dual energy CT scanners with sandwich detectors, though the filter material may have to be reselected.

Conversion gain and charge collection efficiency of detectors are different for high and low energy x-ray data. This difference is compensated by a series of correction operations performed separately for high and low energy x-ray data before input to the dual energy decomposition. The series of correction operations include offset correction, air correction, and monitor correction. The relatively lower collection efficiency of the low-energy projections leads to noise in the photoelectric image, which is compensated for by the adaptive filter and the destreaking algorithms.

Although the image quality of the Z images has been improved significantly using the described methods in this paper, the Z images still yields much lower image quality than the CT images due to the weak photoelectric effect in the total detected x-ray signal. For the purpose of object segmentation, the CT images are used as a primary source, while the Z images are used as a secondary source.

The dual energy CT scanner using the techniques described in this paper has passed the TSA explosive detection certification test with a lower false alarm rate than a comparable single energy CT scanner, demonstrating the effectiveness and sufficiency of our dual energy techniques for explosive detection. However, it is difficult to directly relate the image quality and the precision of the measurements to the performance of the explosive detection.

The methods presented in this paper may not provide optimal solutions to the problems addressed in this paper. However, it is the authors' belief that the methods presented in the paper will shed a light for

future improvement and further investigation into dual energy computed tomography techniques for the detection of explosives and other prohibited materials.

5. Conclusion

In this paper we have presented our dual energy CT techniques applied to explosive detection, including constrained dual energy decomposition, adaptive scatter correction, nonlinear filtering of decomposed projections (destreaking), and real-time image-based correction for x-ray spectral drifts. Experimental results using simulated and real data have demonstrated that the constrained decomposition method reduces approximation and boundary constraint errors; the adaptive scatter correction and destreaking algorithms improve the quality of atomic number images for explosive detection in terms of mean atomic number, cupping effect, and signal to noise ratio; the image-based spectral correction method compensates the atomic number measurement for the spectral drift of the scanner. Further extensions of the work including optimizing dual x-ray energies including HVPS waveforms for explosive detection and correcting heavy metal artifacts in the atomic number image are under investigation.

Acknowledgments

The authors thank Ibrahim Bechwati, Anton Deykoon, Joel Robie, David Rozas, Sergey Simanovsky, and Chitra Subramanian for many helpful discussion and much assistance during scanning and testing. The authors also thank Matthew Hirsch, Alex Roshi, and Ruijuan Ruan for proofreading the manuscript.

Appendix 1: Dual energy CT scanner

The CT scanner used for developing the dual energy techniques described in this paper is a commercial 24-row, third-generation scanner (Model AN6400, Analogic Corporation, Peabody, MA), specifically designed for checked luggage screening. The dual energy data acquisition uses the x-ray source spectrum switching mechanism [20]. The voltage $V(t)$ generated by a high voltage power supply (HVPS) and applied to the x-ray tube for generating dual energy x-ray spectra is a sinusoidally modulated waveform, defined as follows:

$$V(t) = V_{dc} + V_{ac} \sin(2\pi ft) \quad (33)$$

where the nominal values are $V_{dc} = 140$ KV, and $V_{ac} = 40$ KV; the waveform frequency $f = 540$ Hz is one half of the view sampling frequency. The high energy views and low energy views are acquired in an alternating fashion; that is, when the sinusoidal modulation wave is in the positive half-cycle, a high energy view of projection data is acquired; when the sinusoidal modulation wave is in the negative half-cycle, a low energy view of projection data is acquired.

Table 7 also shows the geometry and reconstruction parameters of the dual energy CT scanner. Note that the multi-slice helical image reconstruction uses the Nutating Slice Reconstruction (NSR) algorithm [46].

Table 7
Scanner geometry and reconstruction parameters

| Parameter | Description |
|------------------------------|---|
| Configuration | Third-generation, multi-slice (24 rows) |
| Source-to-isocenter distance | 833.4 mm |
| Source-to-detector distance | 1326.26 mm |
| Field of view | 850 mm diameter |
| Rotation speed | 90 RPM |
| Conveyor belt speed | 150 mm/sec |
| Number of detectors | 252 detectors \times 24 rows |
| Number of views/rotation | 360 high energy and 360 low energy |
| Pixel size | 2 mm \times 2 mm |
| Slice spacing | 3.33 mm |

Appendix 2: Computing Z images

In this appendix we describe how we compute the Z (effective atomic number) image for explosive detection. The dual energy CT scanner generates dual energy projections. We use the high energy projection to reconstruct a CT image for explosive detection. We use the decomposed photoelectric projection to reconstruct a photoelectric image, and use the CT image and the photoelectric image to compute a Z image.

The effective atomic number is the estimate of the hypothetical single element with the same density that will give the same x-ray attenuation as the substance being evaluated. Given the material's composition, the effective atomic number is defined as follows [11,12,47]:

$$Z_{\text{eff}} = \left(\frac{\sum_i \frac{Z_i/A_i}{\sum_j Z_j/A_j} Z_i^n}{\sum_j Z_j/A_j} \right)^{\frac{1}{n}} \quad (34)$$

where i (or j) is the index of the individual element in the composition, Z_i is the atomic number of the individual element in the composition, and A_i is the atomic weight of the individual element in the composition.

Given the measurements of Compton coefficient a_c and photoelectric coefficient a_p , the effective atomic number, denoted as Z_{ac} , can be calculated as follows [14]:

$$Z_{\text{ac}} = K' \left(\frac{a_p}{a_c} \right)^{\frac{1}{n}} \quad (35)$$

where K' and n are constants. The value of n has been a subject of controversy in the literature, but is generally agreed to be between 3 and 4 [17,48].

However, using Eq. (35) for calculating the effective atomic number requires two back-projections, one for the Compton image and the other for the photoelectric image. The back-projection is one of the most computationally intensive modules in the CT reconstruction. It is not practical for a reconstruction system to have two back-projections for the atomic number image and one back-projection for the CT image from cost and system complexity point of views.

In order to reduce the computational cost, we use the CT image to replace the Compton image in computing the effective atomic number, denoted as Z_{hct} , as follows:

$$Z_{\text{hct}} = K \left(\frac{a_p}{a_{\text{hct}}} \right)^{\frac{1}{n}} \quad (36)$$

where K and n are constants, and a_{hct} is the CT number of the scanned materials.

Since the Z image is computed by dividing the photoelectric image by the high energy CT image, the partial volume effect is canceled out in the Z image. This is an important feature for sheet explosive detection.

Appendix 3: Specira generation

The x-ray spectra used for dual energy decomposition on all scanners were simulated according to the scanner's design specification. The energy-dependent attenuation coefficients for the filtration in the beamline were obtained using the XCOM program [49]. The filtration in the beamline for the dual energy scanner described in Appendix 1 includes 0.2 mm thick beryllium, 0.5 mm thick steel, 1.524 mm thick tunnel graphite, and 4.318 mm thick tunnel foam (C_2H_4).

The x-ray beam spectra were modeled using the XSPECW2 program [50], which generates an x-ray spectrum corresponding to an input of the DC voltage. We discretized one cycle of the sinusoidal HVPS voltage into 100 samples. For each sample of the voltage, XSPECW2 was used to generate a spectrum. The 50 x-ray spectra corresponding to the negative sinusoidal waveform were averaged to generate the low energy spectrum, and the 50 x-ray spectra corresponding to the positive sinusoidal waveform were averaged to generate the high energy spectrum. The final x-ray spectra used in our decomposition are shown in Fig. 5. Note that the spectra in the figure are normalized, i.e., $\sum_E S(E) = 1$.

References

- [1] US PUBLIC LAW 107-71-NOV. 19, 2001, *Aviation and Transportation Security Act*.
- [2] K.R. Peschmann and J. Harmann, *Automatic Concealed Object Detection System Having a Pre-Scan Stage*, US Patent 5,182,764, January 26, 1993.
- [3] G. Fenkart, F. Mesqui, D.E. Kresse and W.H. Baylis, *Nonintrusive Inspection System*, US Patent 6,430,255, August 6, 2002.
- [4] K.D. Krug, J.A. Stein and L.A. Taylor, *Device and method for inspection of baggage and other objects*, US Patent 5,319,547, June 7, 1994.
- [5] K.D. Krug, W.F. Aitkenhead, R.F. Eilbert, J.H. Stillson and J.A. Stein, *Identifying explosives or other contraband by employing transmitted or scattered x-rays*, US Patent 5,974,111, October 26, 1999.
- [6] C.R. Crawford and C. Ruth, *Computed tomography scanning target detection using target surface normals*, US Patent 5,901,198, May 4, 1999.
- [7] S. Simanovsky, I.M. Bechwati, M. Hiraoglu and C.R. Crawford, *Apparatus and method for detecting sheet objects in computed tomography data*, US Patent 6,026,143, February 15, 2000.
- [8] S. Singh and M. Singh, Explosives detection systems (EDS) for aviation security, *Signal Processing* **83** (2003), 31–55.
- [9] R.R. Eilbert and K.D. Krug, Aspects of image reconstruction in Vivid Technology's dual-energy x-ray system for explosives detection, in *Proceedings of SPIE* **1824** (1992), 127–143.
- [10] X. Shi, *Improving object classification in x-ray luggage inspection*, Ph.D. dissertation, Virginia Polytechnic Institute and State University, February 2000.
- [11] J. Weber and D.J. van den Berge, The effective atomic number and the calculation of the composition of phantom materials, *The British Journal of Radiology* **42**(497) (May 1969), 378–383.
- [12] E.C. McCullough, Photon attenuation in computed tomography, *Med Phys* **2**(6) (Nov/Dec 1975), 302–315.
- [13] C.A. Wilke, *Leveraging Technology to Improve Aviation Security, Part II*, US Congress Hearing, Committee on Homeland Security, Subcommittee on Economic Security, Infrastructure Protection, and Cybersecurity, July 19 2005.
- [14] R.E. Alvarez and A. Macovski, Energy selective reconstructions in x-ray computed tomography, *Phys Med Biol* **21**(5) (1976), 733–744.
- [15] C.K. Wong and H.K. Huang, Calibration procedure in dual-energy scanning using the basis function technique, *Med Phys* **10**(5) (Sep/Oct 1983), 628–635.
- [16] K.S. Chuang and H.K. Huang, A fast dual-energy computational method using isotransmission lines and table lookup, *Med Phys* **14**(2) (Mar/Apr 1987), 186–192.

- [17] P. Engler and W.D. Friedman, Review of dual-energy computed tomography techniques, *Materials Evaluation* **48** (May 1990), 623–629.
- [18] P. Sukovic and N.H. Clinthorne, Penalized weighted least-squares image reconstruction for dual energy x-ray transmission tomography, *IEEE Trans Med Imag* **19**(11) (November 2000), 1075–1081.
- [19] J.A. Fessler, I. Elbakri, P. Sukovic and N.H. Clinthorne, Maximum-likelihood dual-energy tomographic image reconstruction, in *SPIE 2002 Medical Imaging 4684: Image Proc* **1** (2002), 38–49.
- [20] B.M. Gordon, H. Weedon, I. Izrailit, T.R. Fox and J.F. Moore, *Dual Energy Power Supply*, US Patent 5,661,774, August 26, 1997.
- [21] R.T. Ritchings and B.R. Pullan, A technique for simultaneous dual energy scanning, *J Comput Assist Tomogr* **3**(6) (December 1979), 842–846.
- [22] R.E. Alvarez, J.A. Seibert and S.K. Thompson, Comparison of dual energy detector system performance, *Med Phys* **31**(3) (March 2004), 556–565.
- [23] L.A. Lehmann, R.E. Alvarez, A. Macovski and W.R. Brody, Generalized image combinations in dual KVP digital radiography, *Med Phys* **8**(5) (Sept/Oct 1981), 859–867.
- [24] W.A. Kalender, W.H. Perman, J.R. Vetter and E. Klotz, Evaluation of a prototype dual-energy computed tomographic apparatus. I. phantom studies, *Med Phys* **13**(3) (May/June 1986), 334–339.
- [25] J.R. Vetter, W.H. Perman, W.A. Kalender, R.B. Mazess and J.E. Holden, Evaluation of a prototype dual-energy computed tomographic apparatus. II. determination of vertebral bone mineral content, *Med Phys* **13**(3) (May/June 1986), 340–343.
- [26] H.N. Cardinal and A. Fenster, An accurate method for direct dual-energy calibration and decomposition, *Med Phys* **17**(3) (May/June 1990), 327–341.
- [27] K.S. Chuang, *Theory and applications of dual energy technique*, Ph.D. dissertation, University of California at Los Angeles, 1986.
- [28] A. Macovski, D.G. Nishimura, A. Doost-Hoseini and W.R. Brody, Measurement-dependent filtering: a novel approach to improved SNR, *IEEE Trans Med Imag* **2**(3) (September 1983), 122–127.
- [29] W.A. Kalender, E. Klotz and L. Kostaridou, An algorithm for noise suppression in dual energy CT material density images, *IEEE Trans Med Imag* **7**(3) (September 1988), 218–224.
- [30] J. Hsieh, Adaptive streak artifact reduction in computed tomography resulting from excessive x-ray photon noise, *Med Phys* **25**(11) (November 1998), 2139–2147.
- [31] B. De Man, J. Nuyts, P. Dupont, G. Marchal and P. Suetens, Metal streak artifacts in x-ray computed tomography: A simulation study, *IEEE Trans Nucl Sci* **46**(3) (June, 1999), 691–696.
- [32] D.P. Bertsekas, *Constrained Optimization and Lagrange Multiplier Methods*, Athena Scientific, January 1996.
- [33] D.P. Bertsekas, *Nonlinear Programming*, Athena Scientific; 2nd edition, September 1999.
- [34] G.H. Glover, Compton scatter effects in CT reconstructions, *Med Phys* **9**(6) (Nov/Dec 1982), 860–867.
- [35] M. Endo, T. Tsunoo, N. Nakamori and K. Yoshida, Effect of scattered radiation on image noise in cone beam CT, *Med Phys* **28**(4) (April, 2001), 469–474.
- [36] P.M. Joseph and R.D. Spital, The effects of scatter in x-ray computed tomography, *Med Phys* **9**(4) (July/Aug 1982), 464–472.
- [37] R. Ning, X. Tang and D. Conover, X-ray scatter correction algorithm for cone beam CT imaging, *Med Phys* **31**(5) (May 2004), 1195–1202.
- [38] F.C. Wagner, A. Macovski and D.G. Nishimura, Two interpolating filters for scatter estimation, *Med Phys* **16**(5) (Sep/Oct 1989), 747–757.
- [39] P.C. Johns and M. Yaffe, Scattered radiation in fan beam imaging systems, *Med Phys* **9**(2) (March/April 1982), 231–239.
- [40] J.A. Seibert and J.M. Boone, X-ray scatter removal by deconvolution, *Med Phys* **15**(4) (Jul/Aug 1988), 567–575.
- [41] J.R. Vetter and J.E. Holden, Correction for scattered radiation and other background signals in dual-energy computed tomography material thickness measurements, *Med Phys* **15**(5) (Sep/Oct 1988), 726–731.
- [42] A.P. Colijn and F.J. Beekman, Accelerated simulation of cone beam x-ray scatter projections, *IEEE Trans Med Imag* **23**(5) (May 2004), 584–590.
- [43] P.L. Meyer, *Introductory probability and statistical applications*, Reading, Massachusetts: Addison-Wesley Publishing Company, 1970, 367.
- [44] J.R. Taylor, *Introduction to Error Analysis*, Mill Valley, California: University Science Books, 1982, 270.
- [45] S.S. Karimi, D. Rozas, S. Simanovsky, I. Bechwati and C.R. Crawford, *Method and apparatus for automatic image quality assessment*, US Patent 6,813,374, November 2, 2004.
- [46] G.L. Larson, C.C. Ruth and C.R. Crawford, *Nutating slice CT image reconstruction apparatus and method*, US Patent 5,802,134, September 1, 1998.
- [47] N.C. Yang, P.K. Lechner and W.G. Hawkins, Effective atomic numbers for low-energy total photon interactions in human tissues, *Med Phys* **14**(5) (Sep/Oct 1987), 759–766.
- [48] R.R. Eilbert, Development and evaluation of simulants for x-ray based explosive detection systems, in *Proceedings of the Second Explosives Detection Symposium & Aviation Security Conference*, November 1996, 49–54.

- [49] M.J. Berger and J.H. Hubbell, *XCOM: Photon Cross Sections on a Personal Computer*, Center for Radiation Research, National Bureau of Standards, May 1987.
- [50] E. de Paula, *XSPEC*, Center for Instrumentation, Dosimetry, and Radiation Protection (CIDRA), 1984.